ACS OMEGA

http://pubs.acs.org/journal/acsodf

Article

In Situ Modification of CuO−Fe_2O_3 by Nonthermal Plasma: Insights into the CO_2-to-CH_3OH Hydrogenation Reaction

Nitesh Joshi and Sivachandiran Loganathan*

Cite This: *ACS Omega* 2023, 8, 13410−13420

Read Online

ACCESS | Metrics & More | Article Recommendations | Supporting Information

ABSTRACT: The hydrogenation of CO_2 to CH_3OH on the binary mixed metal oxides of CuO−Fe_2O_3 under nonthermal plasma discharge has been reported in this study. The catalysts are synthesized using the sol−gel route and characterized by XRD, FTIR, SEM, and XPS techniques. The impact of CuO mixing with Fe_2O_3 on CO_2 conversion and CH_3OH yield has been investigated. Herein, we have compared two distinct techniques, namely thermal and plasma catalytic processes. The overall outcome shows that the CO_2 conversion and CH_3OH production increase with an increase in CuO mixing with Fe_2O_3. The synthesized catalyst does not show significant CO_2 conversion and CH_3OH formation in the thermal catalytic process (100−250 °C). Interestingly, when plasma discharge is combined with thermal heating, CO_2 conversion and CH_3OH production significantly improve. The plasma discharges in the CO_2/H_2 gas stream, at low temperatures (<200 °C), reduce Cu^{+2} to Cu^{+1} and Fe^{+3} to Fe^{+2}, which could probably enhance the CO_2 conversion and CH_3OH production. Among the catalysts prepared, 15% CuO−Fe_2O_3 exhibited the best catalytic activity with 13.2% CO_2 conversion, 7.3% CH_3OH yield, and a space−time yield of 13 $mmol_{CH3OH}/h\ g_{cat}$, with 4.67 kJ/L of specific input energy (SIE). The CH_3OH space−time yield is 2.9-fold higher than that of the commercial catalyst Cu/ZnO/Al_2O_3, which is operated at 30 °C with 45.45 kJ/L SIE.

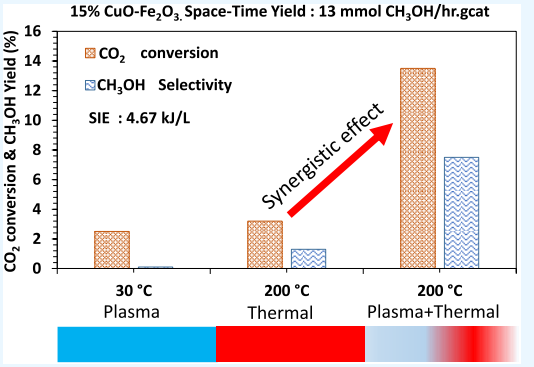

INTRODUCTION

The CO_2 levels are rising globally and have reached above 400 ppm.[1] The capture and conversion of CO_2 as the feedstock for the synthesis of value-added chemicals and fuels is an exciting approach to combat the surge in CO_2 levels in the atmosphere. CO_2 can be converted to various products like urea,[2] polymers,[3] oxygenates such as CH_3OH,[4] C_2H_5OH,[5] CH_4,[6] and synthesis gas,[7] and more importantly, gasoline fractions.[8] There are several technologies for CO_2 conversion, such as photochemical, biochemical, catalysis, electrochemical, plasma catalysis, and solar thermochemical systems.[9−14] As CO_2 is a stable molecule, most of the products obtained from CO_2 are synthesized at high operating pressures and temperatures. Therefore, there is a need to develop technologies that could produce value-added products from CO_2 using economically viable procedures under ambient conditions.

Nonthermal plasma (NTP)-based processes are proven effective for CO_2 conversion to value-added chemicals under ambient conditions.[15,16] The NTP has attracted great interest owing to facilitating thermodynamically unfavorable chemical reactions (such as CO_2 activation) at low temperatures. Although significant efforts have been made to improve the process performance (high CO_2 conversion with better energy efficiency),[9,17−21] product separation is a significant disadvantage from an industrial perspective.

The NTP catalysis is interesting as it operates at a completely different mechanism of electron impact dissociation and, thus, consumes lower energy as compared to thermal catalysis.[22] In thermal catalysis, the vibrational excitation of molecules is a key step that requires higher energy and, thus, affects the overall energy efficiency.[6] Several types of plasma discharges are reported for CO_2 conversion, like glow discharges, corona discharges, radio frequency discharges, microwave discharges, gliding arc discharges, micro-hollow cathode discharges, and DBDs (dielectric barrier discharges).[23−27] Interestingly, except DBD, all other plasmas yield CO as the main product. Remarkably, DBD is also proven to produce oxygenates, namely CH_3OH, C_2H_5OH, CH_3COOH, and other products with the aid of catalysts.[20,28]

CH_3OH is a liquid at room temperature, unlike other high energy density gases like liquefied petroleum gas (LPG), CH_4, and dimethyl ether (DME). Therefore, it does not require any sophisticated storage units. Thus, CH_3OH is widely used as a

Received: February 11, 2023
Accepted: March 21, 2023
Published: March 29, 2023

raw material for preparing gasoline, used as fuel blends, and for generating energy. CH_3OH is produced via various methods like direct CO_2 conversion to CH_3OH over a heterogeneous catalyst,[29,30] steam reforming[31] and dry reforming of CH_4 with CO_2,[32] and hydrogenation of CO.[33] With the said and referred, the need of the century is to convert CO_2 to CH_3OH at atmospheric pressure and temperature compared to industry standards. Using plasma, researchers have tried CO_2 hydrogenation to CH_3OH at atmospheric pressure using 96 kJ/L of specific input energy (SIE) at 50 °C ($3H_2$:CO_2) but could obtain only 0.2% CH_3OH selectivity.[34] Moreover, the increase in reaction temperature has reduced the CH_3OH yield to <0.1%. With the incorporation of Cu/ZnO/Al_2O_3 (CZA) (with 8 bar, 100 °C, and 60 kJ/L of SIE), CH_3OH selectivity was increased to 7−10%, with 12% CO_2 conversion, which corresponds to 0.84−1.2% of CH_3OH yield.[35]

CuO/γ-Al_2O_3 catalyst-coupled high-frequency plasma (9 kHz, SIE = 15 kJ/L) exhibited about 11.3% CH_3OH yield with 21.2% CO_2 conversion.[16] Our previous study demonstrated that a 5 wt % CuO−Fe_2O_3/QW-packed plasma DBD reactor with 1.2 kJ/L of SIE at 200 °C exhibited 16% CO_2 conversion and 5.2% CH_3OH yield.[4] In another study, 10 wt % NiO−Fe_2O_3 showed about 6.2% CO_2 conversion and 6% CH_3OH yield with 2.4 kJ/L of SIE at 200 °C.[36] On investigation, the Co_xO_x/MgO catalytic system reached 33% CO_2 conversion and 10.2% CH_3OH yield using 15 kJ/L of SIE.[37] More recently, Han et al.[38] carried out highly selective CO_2 conversion to CH_3OH. The authors have used CuZnO−ZrO_2 catalyst modified by glow discharge plasma. The modified catalyst, under thermal catalysis (250 °C and 20 bar), exhibited 14.2% CO_2 conversion and CH_3OH yield and selectivity of 11.3 and 78.2%, respectively.

It is well proven that Cu-based catalysts are active toward CO_2 to oxygenate synthesis. In this study, we have investigated the role of mixed oxides CuO−Fe_2O_3 on CO_2 conversion and CH_3OH production under DBD plasma. The synthesized catalysts were systematically characterized by XRD, XPS, SEM, BET surface area analysis, and the basicity of the catalysts (via CO_2-TPD studies). The synergistic effect between plasma discharge and thermal catalysis has been explored. The influence of plasma input energy on CO_2 conversion and product distribution was also investigated.

RESULTS AND DISCUSSION

Catalyst Characterization. The powder XRD patterns of pure CuO and the binary mixed metal oxides of CuO−Fe_2O_3 catalysts are presented in Figure 1. CuO exhibits two intense peaks at 2θ values of 35.5° and 38.5°, which are attributed to the (−002) and (111) planes according to the ICCD database reference number 00-001-1117. In the binary mixed oxides, the characteristic peak at 38.5° was used to calculate the crystallite size of CuO. The peak centered at 35.6° was used to calculate the Fe_2O_3 crystallite size. It was observed that the resultant peak from CuO for mixed metal oxides was very small due to the low mixing amount. With an increase in mixing from 5 to 15%, the characteristic peak at 38.5° shifted to a lower 2θ value. This could be due to the possible intercalation of CuO with the Fe_2O_3 lattice. In addition, with 15% CuO−Fe_2O_3 mixing, the diffraction pattern matches the $CuFeO_2$ spinel structure (ICCD database number 00-021-0290) and $CuFe_2O_4$ structure. This is due to the start of the spinel (normal and inverse spinels) formation when the metal ion ratio reaches close to the 1:2 ratio. Thus, in 15% CuO−Fe_2O_3 binary mixed metal oxide, there could be a mixture of spinels and individual metal oxides, as the perfect ratio of metals for spinel formation is not achieved.

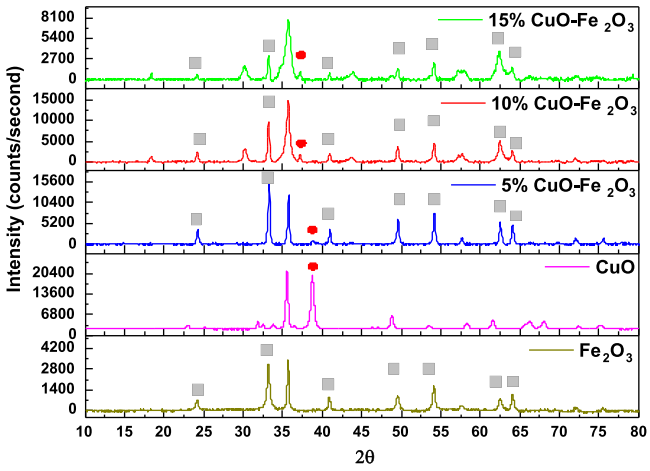

Figure 1. XRD diffraction patterns of CuO and CuO−Fe_2O_3 binary mixed catalysts.

Table 1 represents the physicochemical characteristics of the catalyst. The Scherrer equation was used to calculate the crystallite size of the pure and mixed metal oxides. The crystallite size of CuO was 31 nm; however, when 5% CuO was mixed with Fe_2O_3, the crystallite size was reduced threefold (11 nm) under similar synthesis conditions. The smaller crystallite size indicates that the CuO crystals are not agglomerated and could be uniformly dispersed on the Fe_2O_3 surface. With an increase in CuO mixing, the crystallite size of CuO increases. This infers that above 5% CuO−Fe_2O_3 mixing, the CuO particles start to adhere to each other. However, the Fe_2O_3 crystallite size has not been significantly affected by CuO mixing, as seen in Table 1.

Table 1. Physicochemical Characterization of the Catalysts

	crystallite size (nm)[a]			
catalyst	CuO	Fe_2O_3	metal loading (%)[b]	BET surface area (m^2/g)[c]
Fe_2O_3		32		NA
CuO	31			NA
5% CuO−Fe_2O_3	11.6	20.9	6.4	6.0
10% CuO−Fe_2O_3	36.8	30.5	12.4	24.1
15% CuO−Fe_2O_3	25.8	35.7	20.5	28.5

[a]Using the Scherrer equation. [b]Using the EDX measurement. [c]Using the BET method.

The HRSEM and EDX analyses for 15% CuO−Fe_2O_3 catalyst are presented in Figure 2. The elemental mapping of 5 and 10% CuO−Fe_2O_3 catalysts is reported in Supporting Information (Figures S1 and S2). The HRSEM images revealed that the particles are spherical and uniformly distributed. The EDX analysis showed that the CuO content in the catalyst was slightly higher than the estimated composition, but it serves our motto. The elemental dispersion is studied via elemental mapping, and all the elements are uniformly distributed and not aggregated, even with high percentages of CuO mixing with Fe_2O_3.

The total surface area measured for 5% CuO−Fe_2O_3 was 6 m^2/g (Table 1). The increase in CuO mixing to 10 and 15% increased the surface area to 24 and 28 m^2/g, respectively.

https://doi.org/10.1021/acsomega.3c00915
ACS Omega 2023, 8, 13410−13420

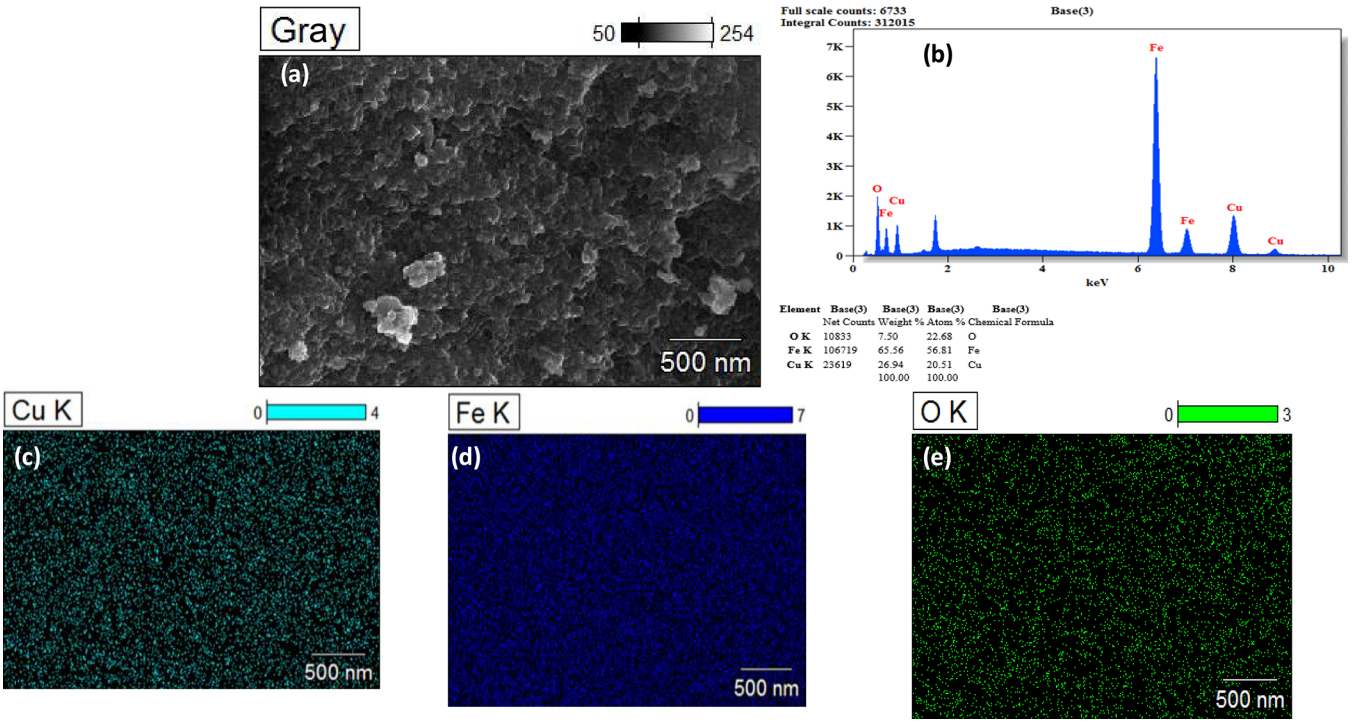

Figure 2. (a) HRSEM image of 15% CuO−Fe_2O_3, (b) EDX compositional details, (c) elemental mapping profile for Cu, (d) elemental mapping profile for Fe, (e) and elemental mapping profile for oxygen.

When CuO was mixed with Fe_2O_3, the total surface area was increased. An increase in the surface area could be correlated to the formation of a new mixed oxide structure. This aligns with the $CuFe_2O_4$ phase observed in XRD (Figure 1). The detailed pore size distribution and N_2 adsorption−desorption profile are reported in Supporting Information (Figures S3−S5).

Evaluating the Distribution of Basic Sites on the Catalyst. The CO_2 adsorption capacity of the fresh catalyst is determined, and the description of CO_2 adsorption experiments is reported in Supporting Information (Figure S6). The CO_2 adsorption capacity of pure CuO and Fe_2O_3 was 141 and 19.4 μmol/g, respectively (Table 2). It was noted that 5% of CuO mixing increased the CO_2 adsorption capacity to 49.5 μmol/g, which is 2.5 times higher than that of fresh Fe_2O_3. However, when CuO mixing increased to 10%, no significant difference in the CO_2 adsorption capacity was observed (50.9 μmol/g). For 15% CuO−Fe_2O_3, the CO_2 adsorption capacity was 86.8 μmol/g. The increase in surface area with the increasing CuO mixing could be attributed to the new porous sites formed, which increases the CO_2 adsorption capacity and eventually could facilitate the CO_2 conversion into CH_3OH.

Table 2. Quantification of the Basic Sites on the Catalyst Surface

catalyst	CO_2 adsorption (μmol/g)	total basic sites (μmol/g)
Fe_2O_3	19.4	17.9
5% CuO−Fe_2O_3	49.2	48.6
10% CuO−Fe_2O_3	50.9	44.9
15% CuO−Fe_2O_3	86.8	78.2
CuO	141.2	137.4

The basic sites on the catalyst surface are quantified by the CO_2-TPD (temperature-programmed desorption) technique. According to the CO_2 desorption temperature, basic sites can be classified into three types: weak sites, medium sites, and strong sites. It is well established that the Lewis basic sites largely control the CO_2 adsorption and subsequent conversion to other products.[39] The weakly adsorbed CO_2 desorbs at temperatures between 25 and 100 °C, moderately adsorbed CO_2 used to desorb temperatures between 100 and 350 °C, and strongly adsorbed CO_2 desorbs between 350 and 800 °C.[40−42] The amount of desorbed CO_2 is directly related to the number of basic sites available on the catalyst surface. It was observed that (Figure 3) pure CuO exhibited a mixture of strong and weak sites favoring CO_2 adsorption. However, on Fe_2O_3, there are a mixture of mild and weak sites for CO_2 adsorption. The strongly adsorbed CO_2 needed high temperature to desorb from the surface. For the Fe_2O_3 catalyst, CO_2 desorption was initiated at 300 °C. In the case of mixed metal oxides, the adsorbed CO_2 molecules are very weak and mild in interaction with the catalyst.

The Lewis and Brønsted basic sites on the catalyst surface are mapped by carrying out CO_2 TPD measurements. The area under the peaks is calculated and added to derive the total basic sites on the catalyst surface. In the synthesized fresh catalyst, Fe_2O_3 possesses 17.9 μmol/g of total basic sites, whereas CuO exhibits a 7.6-fold higher distribution of basic sites on the catalyst surface compared to the Fe_2O_3 catalyst. The mixed metal oxides synthesized show the intermediate distribution of basic sites which increases with an increase in CuO mixing with Fe_2O_3.

Effect of Catalyst Packing on Plasma Discharge Characteristics. Table 3 presents the plasma discharge characteristics of empty, QW (quartz wool), and catalyst sandwiched in QW-DBD reactors. The details of the calculation are presented in Supporting Information (Figure S7). The gas-burning voltage is the minimum voltage which will suffice to decompose a gas molecule. Upon the application

https://doi.org/10.1021/acsomega.3c00915
ACS Omega 2023, 8, 13410−13420

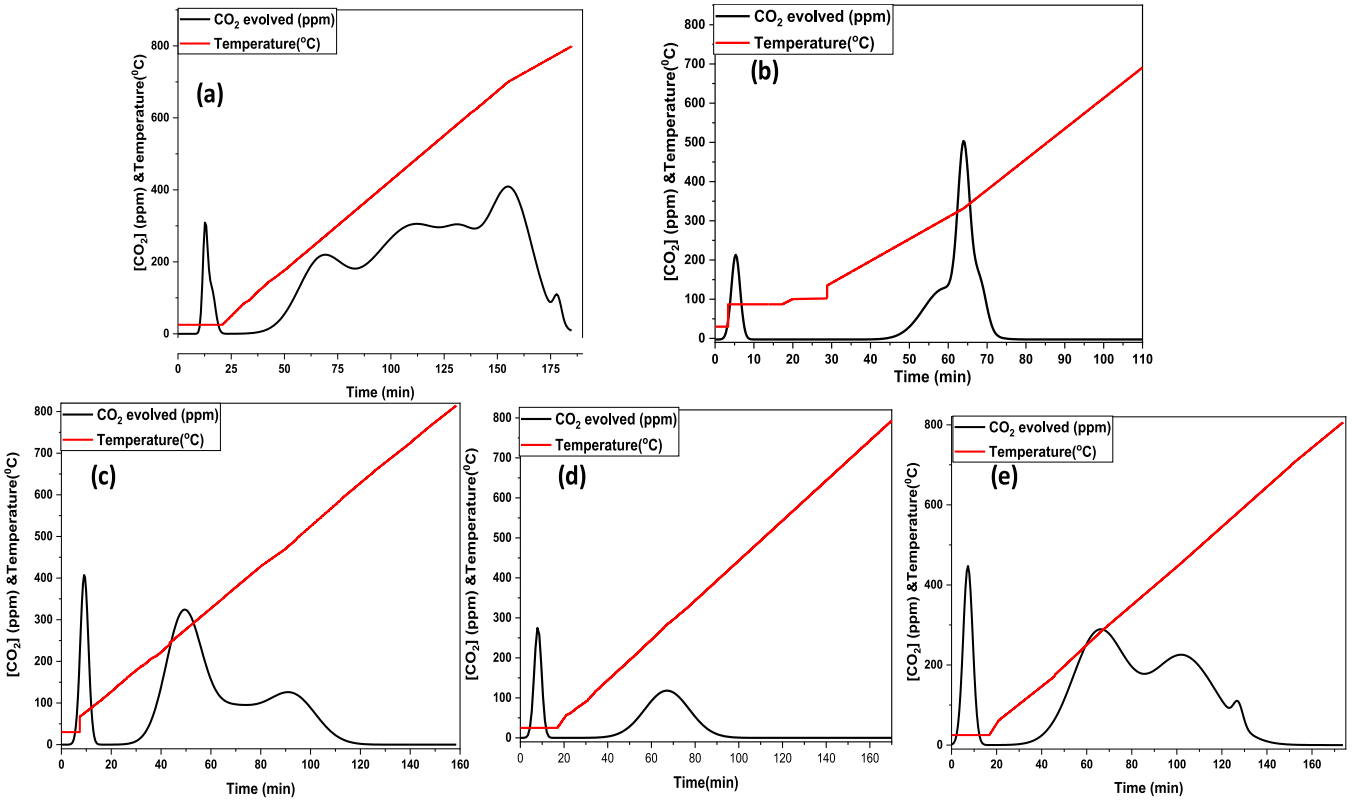

Figure 3. CO_2-TPD profiles of synthesized catalysts: (a) CuO, (b) Fe_2O_3, (c) 5% CuO−Fe_2O_3, (d) 10% CuO−Fe_2O_3, and (e) 15% CuO−Fe_2O_3.

Table 3. Plasma Discharge Characteristics of the DBD Reactor

	temperature (°C)	applied voltage (kV)	burning voltage (kV)	breakdown voltage (kV)	effective capacitance (nC)	Q_{pk-pk} (μC)	dQ (nC)	Q_d (μC)
empty	30	16	0.83	0.52	0.48	24.0	11.5	89.4
	200	16	0.48	0.40	0.53	24.0	8.87	59.8
QW	30	16	0.84	0.47	0.44	22.0	13.8	93.7
	200	16	0.63	0.15	0.70	25.1	12.6	59.4
15% CuO−Fe_2O_3	30	16	1.73	0.41	0.60	26.3	13.2	89.6
	200	16	1.61	0.40	0.78	34.4	17.2	55.3

of external thermal heat, the burning voltage is significantly decreased. Similarly, the breakdown voltage, the minimum energy required to cause ionization, is reduced with external heat. This could be due to the additional energy gained by molecules by external heat, which increases their energy population in the excited states. Thus, they were ionized/decomposed easily. The effective capacitance (reactor capacitance) is, as given in eq 1, equal to dielectric capacitance for a fully packed system.[43] For the empty and QW-packed reactors, the effective capacitance does not vary much, which could be due to the similar total dielectric constant of the reactor and packing material. However, for the 15% CuO−Fe_2O_3 packed reactor, the effective capacitance increases from 0.60 (30 °C) to 0.78 (200 °C); this could be attributed to the additional capacitance from the catalyst.

The external heating decreases the burning voltage and increases the effective capacitance, for all the three configurations investigated, owing to the increase in dielectric constant. As the charge accumulation increases with temperature, the charge injection per cycle (Q_{pk-pk}) and half-cycle (dQ) are also increased. The frequency of the charge−discharge cycle is also increased with external heating. This could be correlated to the improved charge accumulation on the dielectric materials.

$$\frac{1}{C_{Reactor}} = \frac{1}{C_{Dielectric}} + \frac{1}{C_{Gas}} \quad (1)$$

Catalytic Conversion of CO_2. For the catalytic conversion of CO_2 to CH_3OH, all the reactions are carried out at atmospheric pressure, with the feed of CO_2 and H_2 in 1:3 ratio in a total feed flow rate of 100 mL/min. The CO_2 conversion was carried out in a QW-packed reactor under ambient conditions (30 °C and 1 atm), but significant CO_2 conversions (<2%) are not attained for all the studied catalysts despite having a good amount of CO_2 adsorption capacity (Table 2). The energy supplied in plasma discharges is insufficient to activate the strongly adsorbed CO_2 on the binary mixed metal oxide catalyst of the CuO−Fe_2O_3 surface. This is in line with the observation seen from CO_2-TPD experiments reported in Figure 3 and Supporting Information (Figure S8a,b). Under similar operating conditions, thermal catalysis was performed at 200 °C, and CO_2 conversion was slightly improved (>4%). CO_2 molecules are strongly adsorbed on these catalysts and do not desorb from the catalyst surface even at 200 °C (Figure 3).

https://doi.org/10.1021/acsomega.3c00915
ACS Omega 2023, 8, 13410−13420

To understand the influence of SIE on CO_2 conversion, the plasma input energy was varied from 0.43 to 4.67 kJ/L (0–18.2 kV) under ambient conditions (30 °C and 1 atm), and the corresponding CO_2 conversion is provided in Supporting Information (Figure S8a). CH_3OH and CO were the main products quantified at the reactor outlet. The detailed product yields, that is, CH_3OH and CO, are reported in Supporting Information (Figures S9a and 10a). The conditions, which yielded the best results, are presented in Figures 4 and 5a,b.

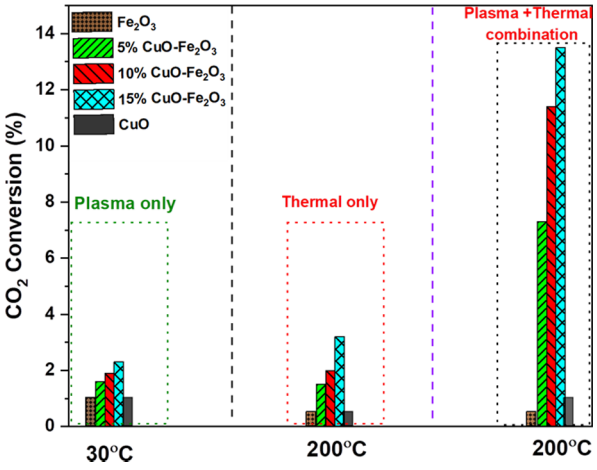

Figure 4. CO_2 conversion as a function of operating parameters for various catalysts. Plasma operating conditions are 18 kV, 50 Hz frequency, and feed flow rate: 100 mL/min SIE 4.67 kJ/L.

The results in Figure 4 are with 7.7 W input power (corresponding to an SIE of 4.67 kJ/L and 18.2 kV of the applied voltage). The CO_2 conversion in plasma catalysis under ambient conditions is 1.7, 1.9, and 2.3% for 5, 10, and 15% of the binary mixed metal oxide of $CuO–Fe_2O_3$ at 4.67 kJ/L of SIE, respectively. Similarly, the CH_3OH yield of <0.1% is obtained for all the catalysts, as seen in Figure 5a. The plasma catalysis shows very low conversion as the catalyst does not reach its optimum catalysis temperature to achieve the best performance. To evaluate the role of the catalyst bed temperature, it is varied from room temperature to 250 °C, which is provided in Supporting Information (Figures S8b, S9b and S10b). When the catalyst bed temperature is 200 °C, the CH_3OH yield and selectivity are at peak compared to other temperatures, as increasing the catalyst bed temperature increases the CO_2 conversion, but CH_3OH production is reduced due to other product formation.

As can be seen from Figure 4, in thermal catalysis at 200 °C, the CO_2 conversion was 1.5, 2 and 3.2% for 5, 10, and 15% of $CuO–Fe_2O_3$, respectively. With the coupling of plasma and thermal heating, the CO_2 conversion is increased to 5.5, 10.9, and 13.5% for 5, 10, and 15% $CuO–Fe_2O_3$ catalyst, respectively. In the absence of thermal heating, that is, in plasma catalysis alone, at 30 °C, the CO_2 conversion was 1.7, 1.9, and 2.3% for 5, 10, and 15% $CuO–Fe_2O_3$ catalyst, respectively. In the coupled study (plasma + thermal heating), the influence of SIE on CO_2 conversion and product distribution is evaluated and provided in Supporting Information (Figures S8c, S9c and S10c). A synergistic effect between plasma discharge and thermal heating is observed for all catalysts investigated in this study.

Figure 5a shows the CH_3OH yield as a function of different operating conditions. The synergistic effect of plasma with thermal heating significantly increased the CH_3OH yield. In plasma catalysis alone, the CH_3OH yield was <0.1%. The rise in the catalyst bed temperature from 30 to 200 °C raises the CH_3OH yield to 1.3% for the 15% $CuO–Fe_2O_3$ catalyst. The CH_3OH yield was five- and sixfold higher than that of thermal and plasma catalysis alone. A maximum of 7.4% CH_3OH yield was obtained for 15% $CuO–Fe_2O_3$; nevertheless, 5.3 and 0.1% CH_3OH yield were obtained for 10 and 5% $CuO–Fe_2O_3$ catalysts, respectively. Thus, it can be concluded that the amount of CuO mixing is beneficial for CH_3OH production and CO_2 activation.

Figure 5b depicts the CO yield quantified at the reactor outlet. CO is produced via the following proposed pathway: (i) CO_2 dissociation induced by electron impact and then dissociation; (ii) reverse water gas shift reaction (RWGS); (iii) partial decomposition of intermediates/products produced during the hydrogenation of CO_2 to CH_3OH. For the catalyst, as shown in Figure 5b, the CO yield increases with an increase in CuO mixing. It is observed that in mixed metal oxides, with an increase in CuO mixing, the CH_3OH as well as CO yield increases. In plasma and thermal catalysis reactions, the CO yield is <1%, which is further increased to 4% in coupled mode. A synergistic effect is observed when plasma and thermal heating is combined for CO_2 conversion and methanol production. This synergistic effect could be

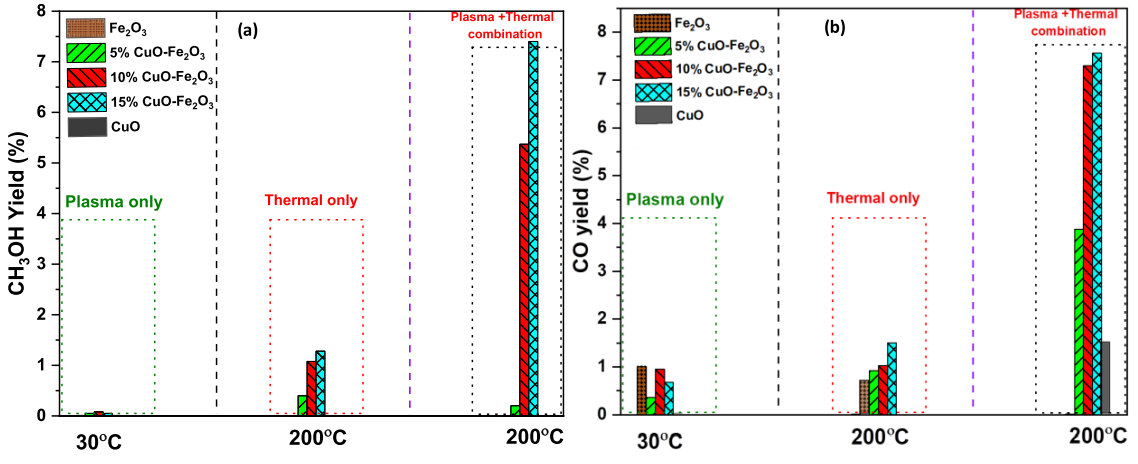

Figure 5. (a) CH_3OH yield as a function of plasma operating parameters. (b) CO yield as a function of plasma operating parameters.

https://doi.org/10.1021/acsomega.3c00915
ACS Omega 2023, 8, 13410–13420

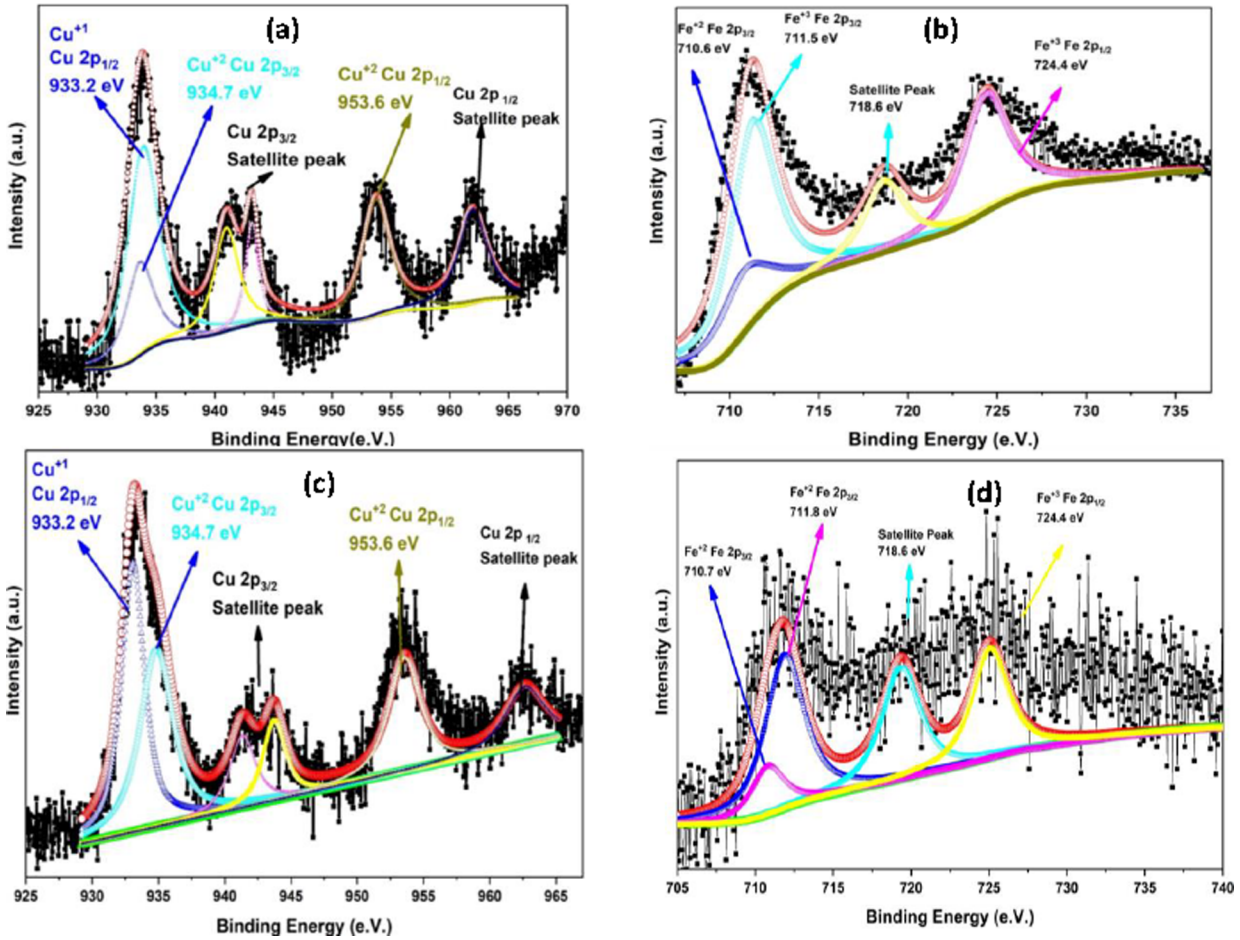

Figure 6. XPS spectra for 15% CuO−Fe_2O_3 before and after the reaction: (a) high resolution XPS for Cu 2p before the reaction, (b) high-resolution XPS for Fe 2p before the reaction, (c) high-resolution XPS for Cu 2p after the reaction, and (d) high-resolution XPS for Fe 2p after the reaction.

correlated to the new crystallite structure, that is, spinel and inverse spinel structure formation, under a reductive plasma atmosphere. Further catalyst surface analysis is needed to support this hypothesis.

The obtained products are in gas phase and need to be separated to make the process efficient. CH_3OH and H_2O could be separated using cooling traps maintained below −70 °C.

Catalyst Modification Induced by Plasma Discharge. The XRD diffraction patterns for the synthesized catalyst and spent catalyst are presented in Supporting Information (Figure S11). It is evidenced that the characteristic peaks for Fe_2O_3 at 33° diminished completely after the plasma-catalytic reaction. This infers that the combined plasma and thermal heating changed the catalyst composition.

The 15% CuO−Fe_2O_3 catalyst yielded the highest CH_3OH yield, and it is further characterized by XPS before (fresh) and after the reaction (used). As can be seen in Figure 6a, the catalyst before the reaction shows the presence of Cu in two oxidation states, namely Cu^{+1} (Cu $2p_{3/2}$ peak at 933.2 eV) and Cu^{+2} (934.7 eV).[44,45] The XPS measurements confirm the presence of $CuFeO_2$ and $CuFe_2O_4$ in the catalyst. In this structure, Cu^{+2} occupies tetrahedral voids, and Fe^{+3} occupies octahedral voids. As reported in Figure 6b, the fresh catalyst exhibits the mixed oxidation states of Fe (+3 and +2). The peak centered at 711.5 eV that resulted from Fe $2p_{3/2}$ is indicative of the Fe^{+3} oxidation state, and the peak centered at 710.6 eV is indicative of the Fe^{+2} oxidation state.[46−49] Therefore, it could be proposed that $CuFe_2O_2$ and $CuFe_2O_4$ are formed after plasma treatment.

Figure 6c shows that the redox couple (Cu^{+2}/Cu^{+1}) equilibrium is shifted in the spent catalyst. As CO_2 hydrogenation is carried out in a reductive atmosphere, it could be expected that CuO, where Cu exists in a +2 state, undergoes reduction to a mixture of +2 and +1 oxidation states. Interestingly, after plasma treatment, the ratio of the $[Cu^{+2}]/[Cu^{+1}]$ redox couple is lowered. The plasma ignition facilitates the reduction process and thus is expected to increase the catalytic activity as the Cu^{+1} state is more active toward CO_2 hydrogenation than Cu^{+2}.[43,50−58] This could be due to the fact that Cu^{+1} sites are important for CO adsorption in the hydrogenation reactions of CO_2 to CH_3OH.[55] More importantly, Cu^{+1} provides stability for intermediates such as carbonates (CO_3^{-2}), formates ($HCOO^-$), and methoxy adsorbates (H_3CO^-) which are formed during CO_2 hydrogenation to CH_3OH due to their higher heats of adsorption.[55]

A similar effect of partial reduction was also seen for the $[Fe^{+3}]/[Fe^{+2}]$ redox couple. As seen from Figure 6d, the spent catalyst shows a lowering in the ratio of the $[Fe^{+3}]/[Fe^{+2}]$ redox couple, which infers the partial reduction of Fe^{+3} to Fe^{+2}.[59]

https://doi.org/10.1021/acsomega.3c00915
ACS Omega 2023, 8, 13410−13420

Table 4. CH_3OH Production and Energy Efficiency for Various Catalysts and Experimental Conditions

catalysts	input power (W)	operating conditions (°C, atm)	Feed flow rate (mL/min)	CO_2 conversion (%)	CH_3OH space time yield (mmol/h g_{cat})	ref
Cu/γ-Al_2O_3	10.0	25, 1	40.0	21.2	0.3	16
CuO/ZnO/Al_2O_3	500.0	200, 8	250.0	11.0	NA	35
Pd/In_2O_3	30.0	25, 1	40.0	24.9	4.5	65
Cu/ZnO/Al_2O_3	30.0		40.0	25.6	4.4	
In_2O_3	30.0		40.0	13.1	1.6	
5% CuO/Fe_2O_3/QW	2.0	200, 1	100.0	16.7	9.3	4
10% NiO−Fe_2O_3	7.2		100.0	6.2	11.9	36
15% Co_xO_y/MgO	10.0	25, 1	28.0	33.0	5.0	37
5% CuO−Fe_2O_3	7.7	200, 1	100.0	7.3	2.06	this work
10% CuO−Fe_2O_3	7.7		100.0	10.9	6.2	
15% CuO−Fe_2O_3	7.7		100.0	18.2	13.0	

CO_2 Activation Reaction Mechanism. In plasma-only conditions, the ignition of plasma with a CO_2/H_2 mixture leads to the dissociation of CO_2 and H_2. CO_2 could be dissociated (electron impact dissociation or via electron impact vibrational excitation) to produce CO. Similarly, H_2 is dissociated by electron impact dissociation to produce hydrogen radicals. Further, several other reactions among radicals could produce formaldehyde (CH_2O). CH_2O hydrogenated to CH_3OH[16,60,61] along with H_2O as a byproduct.[3]

The heterogeneous catalyst surface in the discharge zone stimulates the adsorption−desorption process, especially the radical and gaseous species in the gas phase undergo recombination and/or quenching phenomena. Plasma-created radicals in the boundary layer near the catalyst surfaces can be adsorbed directly, and this will likely require much lower energy.[62−64] CO formed in the plasma gas-phase reactions can be directly adsorbed onto the catalyst surface, which is unique in the plasma-catalytic CO_2 hydrogenation process.

In the coupled mode, that is, plasma catalysis with thermal heating, enhancement in the reactor performance is observed. It could be stated that the population distribution of CO_2 molecules in the vibrationally excited state was much higher than that of a plasma catalyst or plasma-only condition carried out at room temperature. Both electron impact dissociation and electron impact vibrational excitation could contribute to CO_2 dissociation. Furthermore, the additional energy supplied in heat increases the reaction rate as the adsorbed species are vibrationally active.

Comparing the CH_3OH Production Efficiency with the Literature. Table 4 shows the CH_3OH space−time yield given as $mmol_{CH3OH}/h\ g_{cat}$ for various catalyst-packed reactors. The CH_3OH yield is normalized with the feed flow rate, the concentration of CO_2, and grams of catalyst used in the study. The CH_3OH production from CO_2 is an exothermic process; thus, Wang et al.[16] have used water as a ground electrode in the DBD reactor to remove the heat produced in the reaction. The removal of heat, one of the products of CO_2 hydrogenation, could drive the reaction forward. Using this setup, 21.2% CO_2 conversion with 11.2% CH_3OH yield was achieved. The CH_3OH space−time yield for the process was 0.3 $mmol_{CH3OH}/h\ g_{cat}$. Men et al.[65] harnessed the oxygen vacancies on the Pd/In_2O_3 catalyst surface, and 8.9% of CH_3OH yield with 24.5% CO_2 conversion was achieved. The corresponding CH_3OH space−time yield was 4.5 $mmol_{CH3OH}/h\ g_{cat}$, whereas the commercial CH_3OH synthesis catalyst Cu/ZnO/Al_2O_3, under similar conditions, delivered a CH_3OH space−time yield of 4.4 $mmol_{CH3OH}/h\ g_{cat}$. In our previous work, we achieved 16.7% CO_2 conversion with 4.4% CH_3OH yield using 5% CuO−Fe_2O_3 loaded on QW. The CH_3OH space−time yield of 9.3 $mmol_{CH3OH}/h\ g_{cat}$ was attained.[4] In another study, 6.6% CO_2 conversion with 6% CH_3OH yield was obtained with a 10% NiO−Fe_2O_3 catalyst, and the corresponding CH_3OH space−time yield was 11.9 $mmol_{CH3OH}/h\ g_{cat}$.[36] In the current study, with an increase in CuO mixing, the CO_2 conversion and CH_3OH yield increased. The CH_3OH space−time yields for 5, 10, and 15% CuO−Fe_2O_3 catalysts are 2.7, 6.2, and 13 $mmol_{CH3OH}/h\ g_{cat}$, respectively. The obtained CH_3OH space−time yield is 2.9-fold higher than that of the commercial catalyst Cu/ZnO/Al_2O_3 operated at 30 °C with 45.6 kJ/L (about 10-fold high energy) SIE.

CONCLUSIONS

In this work, we have successfully shown that CO_2 could be converted to CH_3OH over CuO−Fe_2O_3 binary mixed metal oxides. It is observed that an increase in CuO mixing with Fe_2O_3 leads to the formation of mixed spinel and inverse spinel, namely $CuFeO_2$ and $CuFe_2O_4$, which is confirmed by XRD and XPS studies. The catalysts exhibited poor performance for CO_2 conversion and CH3OH production in plasma catalysis and thermal catalysis alone due to insufficient energy. However, when the plasma discharge and external thermal heating are combined, significant enhancement in CO_2 conversion and CH_3OH production is observed. The detailed investigation of catalysts, before and after the reaction, reveals that plasma in combination with heating leads to a partial reduction of Cu^{+2} to Cu^{+1} and Fe^{+3} to Fe^{+2}. These in situ changes lead to enhancement in CO_2 conversion and CH_3OH production. The 15% CuO−Fe_2O_3 catalyst is the best catalyst with 13 $mmol_{CH3OH}/h\ g_{cat}$ CH_3OH space−time yield, which is about 2.9-fold higher than the values reported in the literature. The energy efficiency could be further improved by packing the catalyst in a different mode in the reactor and optimizing the experimental conditions.

EXPERIMENTAL SECTION

Catalyst Synthesis. The sol−gel process was used to synthesize the catalysts, and the detailed procedure is reported elsewhere.[4] In brief, various amounts of $Cu(NO_3)_2{\cdot}3H_2O$ were combined with $Fe(NO_3)_3{\cdot}9H_2O$ and dissolved in 50 mL of ethanol. 10% of NH_4OH solution was added at the rate of 1 mL/min to complete the precipitation (pH = 12), and the sol was aged overnight at 85 °C. The excess NH_4OH residue was washed with distilled water and then centrifuged at 7000 rpm

https://doi.org/10.1021/acsomega.3c00915
ACS Omega 2023, 8, 13410−13420

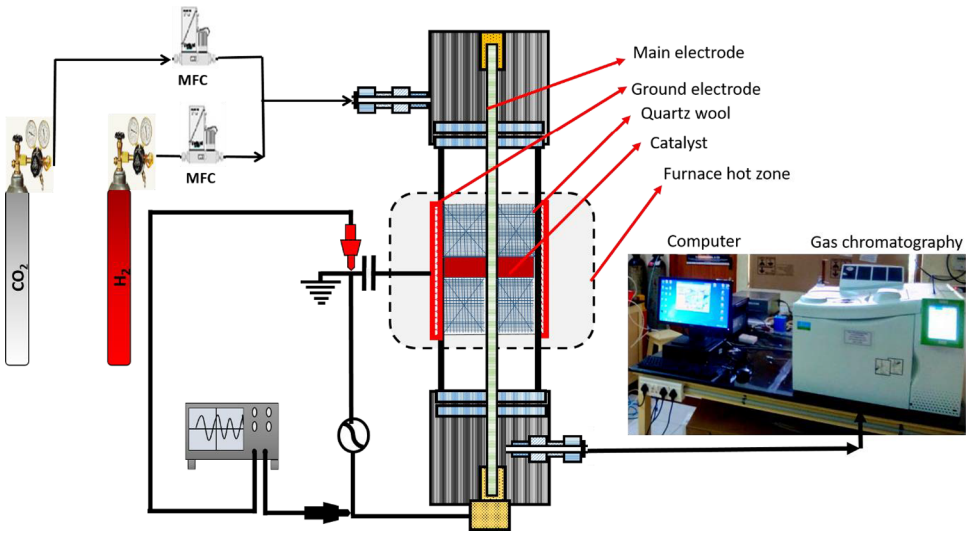

Figure 7. General schematic of the experimental setup. (Photograph courtesy of Nitesh Joshi.)

for 10 min. The washed sol was dried at 100 °C for 6 h and then calcined at 600 °C for 6 h.

Instrumentation Technique. The XRD results are collected using a PANalytical X'pert3 equipment [Cu Kα 1.54 Å, 40 kV, 40 mA]. The nanoscale pictures generated by a high-resolution field emission electron microscope (FESEM, Quanta 200) and a high-resolution transmission electron microscope (HRTEM JEOL, Japan) were used to study the catalyst surface morphology. PHI Versaprobe III was used for the X-ray photoelectron spectroscopy (XPS) study to provide further information on the catalyst's elemental composition and oxidation state. The catalysts' total surface area (BET) was evaluated using an Autosorb iQ Station at 77 K by N_2 physisorption. The catalysts were degassed for 3 h before the analysis in a He atmosphere at 150 °C. CO_2 adsorption and CO_2 TPD were carried out using a homemade setup, as shown in Supporting Information (Figure S5). The CO_2 sensor (model: CM-0121, 100% CO_2 sensor) COZIR 100% was used to monitor the CO_2 concentration.

CO_2 Adsorption–Desorption Experiments. The CO_2 adsorption–desorption experiments were carried out using the setup shown in Figure S5. A mixture of 10% CO_2 + 90% N_2 was first passed through a bypass (without a reactor) to validate the mixture concentration; later, the mixture was passed through the reactor, which housed a catalyst (0.3 g). After reaching the CO_2 adsorption/desorption equilibrium, at room temperature, the streamflow was switched to pure N_2 to remove the weakly adsorbed CO_2 from the catalyst surface. For estimating the concentration of basic sites on the catalyst surface, the catalyst bed temperature was linearly increased to 800 °C (monitored with an external thermocouple) with a ramp of 5 °C/min, and the temporal evolution of CO_2 desorption was monitored using a CO_2 sensor. A more detailed experimental procedure is reported elsewhere.[66]

Plasma Reactor and the Experimental Setup. The general schematic for the experimental system is illustrated in Figure 7. The coaxial tubular reactor is made up of a 600 mm long quartz tube with a 25 mm outer diameter (OD), a 3 mm wall thickness, and a 19 mm inner diameter (ID). A stainless steel rod was housed in a quartz tube, which served as an inner electrode and resulted in a 3.5 mm discharge gap. A 100 mm stain steel mesh was wrapped around the quartz tube and acted as a ground electrode, resulting in a 17.4 cm^3 discharge volume and a gas residence time of 10.4 s^{-1}. A step-up transformer provided by the Jayanti transformer was used to generate the plasma discharge (Chennai, India). The transformer runs at a constant frequency of 50 Hz, and the applied voltage could be adjusted between 0 and 40 kV (peak to peak). As shown in Figure 7, two high voltage probes (HV) with a 1:100 attenuation were used to measure the applied and discharge voltages. The HV probes were connected to an oscilloscope (Keysight, 70 MHz 2 Ga/s) which monitored the input signal from the probes. The Lissajous technique is used to compute the power dissipated in the reactor.[67,68]

Gas-Phase Characterization/Quantification. For all the experiments, the CO_2-to-H_2 mixing ratio was set as 1:3, and the total flow was also fixed at 100 mL/min using precalibrated KOFOLOC mass flow meters, as shown in Figure 7. Before and after the experiment, the gaseous products at the reactor outlet were analyzed using online gas chromatography. The reactor outlet was connected to the gas-sampling loop (2 mL). The TCD detector connected to the ShinCarbon ST column (mesh size of 100/120, length of 2 m, and an inner diameter of 1/11th inch are employed for eluting the reactants and the products) was used for product identification and quantification.

The reaction output, such as CO_2 conversion, product selectivity, yield, and energy efficiency, were calculated using the following equations.

$$\text{Conversion of } CO_2\ (\%) = \frac{[CO_{2(in)} - CO_{2[out]}]}{[CO_{2(in)}]} \times 100 \quad (2)$$

$$\text{Selectivity of CO}\ (\%) = \frac{[CO]}{[CO_{2(in)} - CO_{2[out]}]} \times 100 \quad (3)$$

$$\text{Selectivity of } CH_4\ (\%) = \frac{[CH_4]}{[CO_{2(in)} - CO_{2[out]}]} \times 100 \quad (4)$$

$$\text{Selectivity of } CH_3OH(\%) = \frac{[CH_3OH]}{[CO_{2(in)} - CO_{2[out]}]} \times 100 \quad (5)$$

https://doi.org/10.1021/acsomega.3c00915
ACS Omega 2023, 8, 13410−13420

$$\text{Yield } (CH_3OH(\%), CO(\%), CH_{4(\%)}) = \frac{[(S_{CH_3OH(\%)}, S_{CO(\%)}S_{CH_4(\%)}) \times X_{CO_2}(\%)]}{100} \quad (6)$$

$$CH_3OH \text{ Space Time Yield } (\text{mmol } h^{-1} \text{ g cat}^{-1}) = \frac{F_{CO_{2\,in}} \times S_{CH_3OH} \times X_{CO_2}}{W_{cat}} \times 1000 \quad (7)$$

S_{CH_3OH} and X_{CO_2} are the selectivity of CH_3OH and conversion of CO_2, respectively. $F_{CO_{2\,in}}$ is the molar flow rate of CO_2, and W_{cat} is the weight of the catalyst.

Experimental Procedure. For all the experiments, that is, plasma, thermal, and plasma + thermal combination, about 0.5 ± 0.05 g of metal oxide was placed in the center of the quartz tube in sandwich mode using quartz wool (3.7 g). Before each experiment, the catalyst was pretreated at 300 °C for 1 h under 100 mL/min of zero air. Then, the reactor was cooled down to room temperature, and the mixture of H_2:CO_2 (3:1) was sent to the reactor inlet. The blank concentrations of CO_2 and H_2 were obtained after reaching the adsorption−desorption equilibrium at the reactor downstream.

For thermal catalysis, the catalyst bed temperature was linearly varied from 100 to 250 °C. The online sampling was carried out after reaching the steady state (60 min of the thermal catalytic process). For each set temperature, a minimum of three samples were analyzed to ensure reproducibility, and a minimum of three experiments were performed to reduce the error percentage.

For the plasma + thermal catalytic process, the plasma discharge was ignited after reaching the thermal catalytic steady state (about 60 min of the thermal catalytic process) with the set temperature. The online sampling is performed after 10 min of continuous plasma treatment. Notably, during the plasma treatment, the furnace was switched off to avoid electrical perturbation. It is observed that the temperature difference, before and after plasma treatment, was less than ±10 °C.

■ ASSOCIATED CONTENT

Supporting Information

The Supporting Information is available free of charge at https://pubs.acs.org/doi/10.1021/acsomega.3c00915.

HRSEM, EDAX, elemental distribution, N_2 adsorption−desorption isotherms, CO_2 adsorption, CO_2-TPD, evaluation of electrical parameters of plasma, CO_2 conversion and product distribution in plasma catalysis, thermal catalysis, and both combined (plasma catalysis + thermal heating), and XRD diffraction data of the fresh and spent catalysts (PDF)

■ AUTHOR INFORMATION

Corresponding Author

Sivachandiran Loganathan − *Laboratory of Plasma Chemistry and Physics (LPCP), Department of Chemistry, Faculty of Engineering and Technology, SRM Institute of Science and Technology, Chennai 603203, India; Plasma Research Laboratory, Department of Chemical and Biomolecular Engineering, and Center for Air and Aquatic Resources Engineering & Science, Clarkson University, Potsdam, New York 13699, United States;* orcid.org/0000-0001-7375-0134; Email: sloganat@clarkson.edu, sivachal@srmist.edu.in

Author

Nitesh Joshi − *Laboratory of Plasma Chemistry and Physics (LPCP), Department of Chemistry, Faculty of Engineering and Technology, SRM Institute of Science and Technology, Chennai 603203, India;* Present Address: School of Chemical Sciences, Goa University, Taleigao Plateau, 403206 Goa, India; orcid.org/0000-0002-3985-6565

Complete contact information is available at: https://pubs.acs.org/10.1021/acsomega.3c00915

Notes

The authors declare the following competing financial interest(s): Science & Engineering Research Board, Department of Science & Technology, Government of India (SERB, File NO. ECR/2016/001457).

■ ACKNOWLEDGMENTS

The authors greatly acknowledge the financial support of the Science and Engineering Research Board, Department of Science and Technology, Government of India (SERB, File NO. ECR/2016/001457). The authors acknowledge SRMIST for the high-resolution scanning electron microscope (HR-SEM) facility. They acknowledge Nanotechnology Research Centre (NRC) and SRMIST for providing the research facilities.

■ REFERENCES

(1) Dlugokencky, E. J.; Hall, B. D.; Montzka, S. A.; Dutton, G.; Mühle, J.; Elkins, J. W. Atmospheric composition (in State of the Climate in 2018, Chapter 2: Global Climate). *Bull. Am. Meteorol. Soc.* **2019**, *100*, 48−50.

(2) Krase, N. W.; Gaddy, V. L. Synthesis of urea from ammonia and carbon dioxide. *Ind. Eng. Chem.* **1992**, *14*, 611−615.

(3) Qin, Y., Wang, X., Conversion of CO_2 into Polymers. In *Green Chemistry and Chemical Engineering*, Encyclopedia of Sustainability Science and Technology Series; Han, B., Wu, T. Eds.; Springer: New York, NY.

(4) Joshi, N.; Loganathan, S. Methanol synthesis from CO_2 using Ni and Cu supported Fe catalytic system: Understanding the role of nonthermal plasma surface discharge. *Plasma Processes Polym.* **2021**, *18*, No. 2000104.

(5) Bai, S.; Shao, Q.; Wang, P.; Dai, Q.; Wang, X.; Huang, X. Highly active and selective hydrogenation of CO_2 to ethanol by ordered Pd−Cu nanoparticles. *J. Am. Chem. Soc.* **2017**, *139*, 6827−6830.

(6) Sivachandiran, L.; Da Costa, P.; Khacef, A. CO_2 reforming in CH_4 over Ni/γ-Al_2O_3 nano catalyst: Effect of cold plasma surface discharge. *Appl. Surf. Sci.* **2020**, *501*, No. 144175.

(7) Futamura, S.; Kabashima, H. Synthesis gas production from CO_2 and H_2O with nonthermal plasma. *Stud. Surf. Sci. Catal.* **2004**, *153*, 119−124.

(8) Wei, J.; Ge, Q.; Yao, R.; Wen, Z.; Fang, C.; Guo, L.; Sun, J. Directly converting CO_2 into a gasoline fuel. *Nat. Commun.* **2017**, *8*, 15174.

(9) Bogaerts, A.; Neyts, E. C. Plasma technology: an emerging technology for energy storage. *ACS Energy Lett.* **2018**, *3*, 1013−1027.

(10) Hashemizadeh, I.; Golovko, V. B.; Choi, J.; Tsang, D. C. W.; Yip, A. C. K. Photocatalytic reduction of CO_2 to hydrocarbons using bio-templated porous TiO_2 architectures under UV and visible light. *Chem. Eng. J.* **2018**, *347*, 64−73.

(11) Vennekoetter, J. B.; Sengpiel, R.; Wessling, M. Beyond the catalyst: How electrode and reactor design determine the product spectrum during electrochemical CO_2 reduction. *Chem. Eng. J.* **2019**, *364*, 89−101.

(12) Zeng, S.; Kar, P.; Thakur, U. K.; Shankar, K. A review on photocatalytic CO_2 reduction using perovskite oxide nanomaterials. *Nanotechnology* **2018**, *29*, No. 052001.
(13) Loutzenhiser, P. G.; Meier, A.; Steinfeld, A. Review of the two-step H_2O/CO_2-splitting solar thermochemical cycle based on Zn/ZnO redox reactions. *Materials* **2010**, *3*, 4922−4938.
(14) Xu, S.; Whitehead, J. C.; Martin, P. A. CO_2 conversion in a nonthermal, barium titanate packed bed plasma reactor: The effect of dilution by Ar and N_2. *Chem. Eng. J.* **2017**, *327*, 764−773.
(15) Michielsen, I.; Uytdenhouwen, Y.; Pype, J.; Michielsen, B.; Mertens, J.; Reniers, F.; Meynen, V.; Bogaerts, A. CO_2 dissociation in a packed bed DBD reactor: First steps towards a better understanding of plasma catalysis. *Chem. Eng. J.* **2017**, *326*, 477−488.
(16) Wang, L.; Yi, Y.; Guo, H.; Tu, X. Atmospheric Pressure and Room Temperature Synthesis of Methanol through Plasma-Catalytic Hydrogenation of CO_2. *ACS Catal.* **2018**, *8*, 90−100.
(17) Chen, G.; Georgieva, V.; Godfroid, T.; Snyders, R.; Delplancke-Ogletree, M.-P. Plasma assisted catalytic decomposition of CO_2. *Appl. Catal., B* **2016**, *190*, 115−124.
(18) Van Rooij, G. J.; Akse, H. N.; Bongers, W. A.; Van de Sanden, M. C. M. Plasma for electrification of chemical industry: a case study on CO_2 reduction. *Plasma Phys. Controlled Fusion* **2018**, *60*, No. 014019.
(19) Chen, G.; Godfroid, T.; Georgieva, V.; Britun, N.; Delplancke-Ogletree, M.-P.; Snyders, R. Plasma catalytic conversion of CO_2 and CO_2/H_2O in a surface-wave sustained microwave discharge. *Appl. Catal., B* **2017**, *214*, 114−125.
(20) Wang, L.; Yi, Y.; Wu, C.; Guo, H.; Tu, X. One-Step Reforming of CO_2 and CH_4 into High-Value Liquid Chemicals and Fuels at Room Temperature by Plasma-Driven Catalysis. *Angew. Chem., Int. Ed.* **2017**, *56*, 13679−13683.
(21) Snoeckx, R.; Bogaerts, A. Plasma technology − a novel solution for CO_2 conversion. *Chem. Soc. Rev.* **2017**, *46*, 5805−5863.
(22) Joshi, N., Sivachandiran, L., Assadi, A.A., Perspectives in advance technologies/strategies for combating rising CO_2 levels in the atmosphere via CO_2 utilisation: A review. In *IOP Conference Series: Earth and Environmental Science*; 2022; Vol. *1100*, p 012020.
(23) Belov, I.; Paulussen, S.; Bogaerts, A. Appearance of a conductive carbonaceous coating in a CO_2 dielectric barrier discharge and its influence on the electrical properties and the conversion efficiency. *Plasma Sources Sci. Technol.* **2016**, *25*, No. 015023.
(24) Van Laer, K.; Bogaerts, A. Improving the conversion and energy efficiency of carbon dioxide splitting in a zirconia-packed dielectric barrier discharge reactor. *Energy Technol.* **2015**, *3*, 1038−1044.
(25) Sentek, J.; Krawczyk, K.; Młotek, M.; Kalczewska, M.; Kroker, T.; Kolb, T.; Schenk, A.; Gericke, K. H.; Schmidt-Szałowski, K. Plasma-catalytic methane conversion with carbon dioxide in dielectric barrier discharges. *Appl. Catal., B* **2010**, *94*, 19−26.
(26) Song, H. K.; Choi, J. W.; Yue, S. H.; Lee, H.; Na, B. K. Synthesis gas production via dielectric barrier discharge over Ni/γ-Al_2O_3 catalyst. *Catal. Today* **2004**, *89*, 27−33.
(27) Kraus, M.; Egli, W.; Haffner, K.; Eliasson, B.; Kogelschatz, U.; Wokaun, A. Investigation of mechanistic aspects of the catalytic CO_2 reforming of methane in a dielectric-barrier discharge using optical emission spectroscopy and kinetic modelling. *Phys. Chem. Chem. Phys.* **2002**, *4*, 668−675.
(28) Li, Y.; Liu, C. J.; Eliasson, B.; Wang, Y. Synthesis of oxygenates and higher hydrocarbons directly from methane and carbon dioxide using dielectric-barrier discharges: product distribution. *Energy Fuels* **2002**, *16*, 864−870.
(29) Chinchen, G. C.; Denny, P. J.; Parker, D. G.; Spencer, M. S.; Whan, D. A. Mechanism of methanol synthesis from $CO_2/CO/H_2$ mixtures over copper/zinc oxide/alumina catalysts: use of14C-labelled reactants. *Appl. Catal.* **1987**, *30*, 333−338.
(30) Huff, C. A.; Sanford, M. S. Cascade catalysis for the homogeneous hydrogenation of CO_2 to methanol. *J. Am. Chem. Soc.* **2011**, *133*, 18122−18125.
(31) Zhang, C.; Jun, K. W.; Gao, R.; Kwak, G.; Park, H. G. Carbon dioxide utilization in a gas-to-methanol process combined with CO_2/Steam-mixed reforming: Techno-economic analysis. *Fuel* **2017**, *190*, 303−311.
(32) Shi, L. E. I.; Yang, G.; Tao, K. A. I.; Yoneyama, Y.; Tan, Y.; Tsubaki, N. An introduction of CO_2 conversion by dry reforming with methane and new route of low-temperature methanol synthesis. *Acc. Chem. Res.* **2013**, *46*, 1838−1847.
(33) Kar, S.; Goeppert, A.; Prakash, G. S. Catalytic homogeneous hydrogenation of CO to methanol via formamide. *J. Am. Chem. Soc.* **2019**, *141*, 12518−12521.
(34) Bill, A.; Eliasson, B.; Kogelschatz, U.; Zhou, L. M. Comparison of CO_2 hydrogenation in a catalytic reactor and in a dielectric-barrier discharge. *Stud. Surf. Sci. Catal.* **1998**, *114*, 541−544.
(35) Eliasson, B.; Kogelschatz, U.; Xue, B.; Zhou, L. M. Hydrogenation of carbon dioxide to methanol with a discharge-activated catalyst. *Ind. Eng. Chem. Res.* **1998**, *37*, 3350−3357.
(36) Joshi, N.; Sivachandiran, L. Exploring the feasibility of liquid fuel synthesis from CO_2 under cold plasma discharge: role of plasma discharge in binary metal oxide surface modification. *RSC Adv.* **2021**, *11*, 27757−27766.
(37) Ronda-Lloret, M.; Wang, Y.; Oulego, P.; Rothenberg, G.; Tu, X.; Shiju, N. R. CO_2 hydrogenation at atmospheric pressure and low temperature using plasma-enhanced catalysis over supported cobalt oxide catalysts. *ACS Sustainable Chem. Eng.* **2020**, *8*, 17397−17407.
(38) Han, F.; Liu, H.; Cheng, W.; Xu, Q. Highly selective conversion of CO_2 to methanol on the CuZnO−ZrO_2 solid solution with the assistance of plasma. *RSC Adv.* **2020**, *10*, 33620−33627.
(39) Khoja, A. H.; Tahir, M.; Amin, N. A. S. Cold plasma dielectric barrier discharge reactor for dry reforming of methane over Ni/γ-Al_2O_3-MgO nanocomposite. *Fuel Process. Technol.* **2018**, *178*, 166−179.
(40) Weng, Y.; Qiu, S.; Ma, L.; Liu, Q.; Ding, M.; Zhang, Q.; Wang, T. Jet-fuel range hydrocarbons from biomass-derived sorbitol over Ni-HZSM-5/SBA-15 catalyst. *Catalysts* **2015**, *5*, 2147−2160.
(41) Zheng, A.; Zhao, Z.; Chang, S.; Huang, Z.; Zhao, K.; Wu, H.; Li, H. Maximum synergistic effect in the coupling conversion of bio-derived furans and methanol over ZSM-5 for enhancing aromatic production. *Green Chem.* **2014**, *16*, 2580−2586.
(42) Hoang, T. Q.; Zhu, X.; Lobban, L. L.; Resasco, D. E.; Mallinson, R. G. Effects of HZSM-5 crystallite size on stability and alkyl-aromatics product distribution from conversion of propanal. *Catal. Commun.* **2010**, *11*, 977−981.
(43) Mei, D.; Zhu, X.; He, Y.-L.; Yan, J. D.; Tu, X. Plasma-Assisted Conversion of CO_2 in a Dielectric Barrier Discharge Reactor:Understanding the Effect of Packing Materials. *Plasma Sources Sci. Technol.* **2015**, *24*, No. 015011.
(44) Xiong, D.; Qi, Y.; Li, X.; Liu, X.; Tao, H.; Chen, W.; Zhao, X. Hydrothermal synthesis of delafossite $CuFeO_2$ crystals at 100 °C. *RSC Adv.* **2015**, *5*, 49280.
(45) Wang, J.; Deng, Q.; Li, M.; Jiang, K.; Zhang, J.; Hu, Z.; Chu, J. Copper ferrites@ reduced graphene oxide anode materials for advanced lithium storage applications. *Sci. Rep.* **2017**, *7*, 8903.
(46) Li, P.; Jiang, E. Y.; Bai, H. L. Fabrication of ultrathin epitaxial γ-Fe_2O_3 films by reactive sputtering. *J. Phys. D: Appl. Phys.* **2011**, *44*, No. 075003.
(47) Biesinger, M. C.; Lau, L. W.; Gerson, A. R.; Smart, R. S. C. Resolving surface chemical states in XPS analysis of first row transition metals, oxides and hydroxides: Sc, Ti, V Cu and Zn. *Appl. Surf. Sci.* **2010**, *257*, 887−898.
(48) Uhlig, I.; Szargan, R.; Nesbitt, H. W.; Laajalehto, K. Surface states and reactivity of pyrite and marcasite. *Appl. Surf. Sci.* **2001**, *179*, 222−229.
(49) Ul Haq, M.; Wen, Z.; Zhang, Z.; Khan, S.; Lou, Z.; Ye, Z.; Zhu, L. A two-step synthesis of nanosheet-covered fibers based on α-Fe_2O_3/NiO composites towards enhanced acetone sensing. *Sci. Rep.* **2018**, *8*, 1705.
(50) Liu, X. M.; Lu, G. Q.; Yan, Z. F.; Beltramini, J. Recent advances in catalysts for methanol synthesis via hydrogenation of CO and CO_2. *Ind. Eng. Chem. Res.* **2003**, *42*, 6518−6530.

https://doi.org/10.1021/acsomega.3c00915
ACS Omega 2023, 8, 13410−13420

(51) Chinchen, G. C.; Waugh, K. C.; Whan, D. A. The activity and state of the copper surface in methanol synthesis catalysts. *Ind. Eng. Chem. Res.* **1986**, *25*, 101−107.
(52) Chinchen, G. C.; Spencer, M. S.; Waugh, K. C.; Whan, D. A. Promotion of methanol synthesis and the water-gas shift reactions by adsorbed oxygen on supported copper catalysts. *J. Chem. Soc., Faraday Trans. 1* **1987**, *83*, 2193−2212.
(53) Szanyi, J.; Goodman, D. W. Methanol synthesis on a Cu (100) catalyst. *Catal. Lett.* **1991**, *10*, 383−390.
(54) Sheffer, G. R.; King, T. S. Potassium's promotional effect of unsupported copper catalysts for methanol synthesis. *J. Catal.* **1989**, *115*, 376−387.
(55) Bailey, S.; Froment, G. F.; Snoeck, J. W.; Waugh, K. C. A DRIFTS study of the morphology and surface adsorbate composition of an operating methanol synthesis catalyst. *Catal. Lett.* **1994**, *30*, 99−111.
(56) Nakamura, J.; Choi, Y.; Fujitani, T. On the issue of the active site and the role of ZnO in Cu/ZnO methanol synthesis catalysts. *Top. Catal.* **2003**, *22*, 277−285.
(57) Sahibzada, M.; Metcalfe, I. S.; Chadwick, D. J. J. O. C. Methanol Synthesis from $CO/CO_2/H_2$ over $Cu/ZnO/Al_2O_3$ at Differential and Finite Conversions. *J. Catal.* **1998**, *174*, 111−118.
(58) Le, M.; Ren, M.; Zhang, Z.; Sprunger, P. T.; Kurtz, R. L.; Flake, J. C. Electrochemical reduction of CO_2 to CH_3OH at copper oxide surfaces. *J. Electrochem. Soc.* **2011**, *158*, E45.
(59) Grosvenor, A. P.; Kobe, B. A.; Biesinger, M. C.; McIntyre, N. S. Investigation of multiplet splitting of Fe 2p XPS spectra and bonding in iron compounds. *Surf. Interface Anal.* **2004**, *36*, 1564−1574.
(60) Aerts, R.; Somers, W.; Bogaerts, A. Carbon dioxide splitting in a dielectric barrier discharge plasma: a combined experimental and computational study. *ChemSusChem* **2015**, *8*, 702−716.
(61) De Bie, C.; van Dijk, J.; Bogaerts, A. CO_2 hydrogenation in a dielectric barrier discharge plasma revealed. *J. Phys. Chem. C* **2016**, *120*, 25210−25224.
(62) Whitehead, J. C. Plasma−catalysis: the known knowns, the known unknowns and the unknown unknowns. *J. Phys. D: Appl. Phys.* **2016**, *49*, No. 243001.
(63) Stere, C. E.; Anderson, J. A.; Chansai, S.; Delgado, J. J.; Goguet, A.; Graham, W. G.; Yang, H. Nonthermal plasma activation of gold-based catalysts for low-temperature water−gas shift catalysis. *Angew. Chem., Int. Ed.* **2017**, *56*, 5579−5583.
(64) Stere, C. E.; Adress, W.; Burch, R.; Chansai, S.; Goguet, A.; Graham, W. G.; Hardacre, C. Probing a non-thermal plasma activated heterogeneously catalyzed reaction using in situ DRIFTS-MS. *ACS Catal.* **2015**, *5*, 956−964.
(65) Men, Y. L.; Liu, Y.; Wang, Q.; Luo, Z. H.; Shao, S.; Li, Y. B.; Pan, Y. X. Highly dispersed Pt-based catalysts for selective CO_2 hydrogenation to methanol at atmospheric pressure. *Chem. Eng. Sci.* **2019**, *200*, 167−175.
(66) Gawas, P.; Joshi, N.; Sivachandiran, L.; Nutalapati, V. CO_2 uptake and storage by small organic functional phenothiazine molecule−An experimental study. *Mater. Sci. Eng.: B* **2022**, *286*, No. 116048.
(67) Butterworth, T.; Elder, R.; Allen, R. Effects of particle size on CO_2 reduction and discharge characteristics in a packed bed plasma reactor. *Chem. Eng. J.* **2016**, *293*, 55−67.
(68) Manley, T. C. The electric characteristics of the ozonator discharge. *Trans. Electrochem. Soc.* **1943**, *84*, 83−96.

https://doi.org/10.1021/acsomega.3c00915
ACS Omega 2023, 8, 13410−13420